Macromolecules

pubs.acs.org/Macromolecules
Article

Structure and Properties of Metallosupramolecular Polymers with a Nitrogen-Based Bidentate Ligand

Franziska Marx, Malte Beccard, Alessandro Ianiro, Andrea Dodero, Laura N. Neumann, Grégory Stoclet, Christoph Weder,* and Stephen Schrettl*

Cite This: *Macromolecules* 2023, 56, 7320–7331
Read Online

ABSTRACT: The solid-state properties of supramolecular polymers that feature metal–ligand (ML) complexes are, in addition to the general nature of the monomer, significantly affected by the choice of ligand and metal salt. Indeed, the variation of these components can be used to alter the structural, thermal, mechanical, and viscoelastic properties over a wide ranges. Moreover, the dynamic nature of certain ML complexes can render the resulting metallosupramolecular polymers (MSPs) stimuli-responsive, enabling functions such as healing, reversible adhesion, and mechanotransduction. We here report MSPs based on the bidentate ligand 6-(1′-methylbenzimidazolyl) pyridine (MBP), which is easily accessible and forms threefold coordination complexes with various transition metal ions. Thus, a poly(ethylene-*co*-butylene) telechelic was end-functionalized with two MBP ligands and the resulting macromonomer was assembled with the triflate salts of either Zn^{2+}, Fe^{2+}, or Ni^{2+}. All three MSPs microphase separate and adopt, depending on the metal ion and thermal history, lamellar or hexagonal morphologies with crystalline domains formed by the ML complexes. The melting transitions are well below 200 °C, and this permits facile (re)processing. Furthermore, defects can be readily and fully healed upon exposure to UV-light. While the three MSPs display similar moduli in the rubbery regime, their extensibility and tensile strength depend on the nature of the ML complex, which similarly affects the long-range order and dynamic behavior.

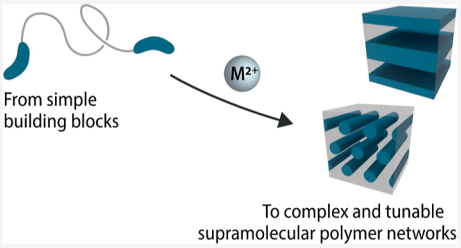

INTRODUCTION

Supramolecular polymers are formed through the self-assembly of (macro)monomers equipped with two or more binding motifs that can form noncovalent bonds through, for example, hydrogen-bonding, host–guest interactions, π-interactions, or metal–ligand complexation.[1−3] The dynamic nature of supramolecular bonds can render these materials responsive to external stimuli such as light or heat,[4,5] which can cause the temporary disassembly into monomeric species and support functions such as healing,[6−9] reversible adhesion,[10,11] recycling,[12,13] and easy (re)processing.[14−16] Metallosupramolecular polymers (MSPs), which feature metal–ligand (ML) complexes as the supramolecular binding motif, represent a subset of this family of materials. The thermodynamic and kinetic attributes of ML complexes, reflected in the association constant and supramolecular bond lifetime, can be tuned very easily by changing the ligand and the metal salt, and this enables tailoring the materials properties over a wide range.[17−21] Furthermore, the coordination geometry of the ML complexes can be used to control the connectivity of the building blocks. For example, bifunctional telechelic macromonomers equipped with ligands that bind metal ions in a 2:1 stoichiometry assemble by means of linear chain extension, while the same macromonomers afford MSP networks if the stoichiometry is 3:1.[22,23] Polarity differences between the ML complexes and the organic residues in the monomers have been observed to lead to microphase separation, and the characteristics of the formed phases, i.e., glassy or crystalline, substantially affect the thermomechanical properties of the MSPs.[24,25]

A plethora of MSPs has been reported, based on ligands that vary greatly in the nature of the donor atom(s) and their denticity,[17,26] although nitrogen-based ligands that carry one or multiple pyridine or imidazole units represent, arguably, the most widely employed binding motif.[27,28] While there are countless MSPs based on (macro)monomers featuring terpyridine or other tridentate nitrogen-based ligands,[29,30] including the widely employed 2,6-bis(1′-methylbenzimidazolyl)pyridine (Mebip),[17,31,32] (macro)monomers with bidentate nitrogen ligands have been studied less frequently, possibly due to their lower binding constants, which can, however, render the corresponding supramolecular systems more dynamic.[33−35] Thus, several examples of MSPs featuring bidentate ligands include building blocks of relatively low-molecular weight, which were assembled into dynamic,

Received: March 20, 2023
Revised: July 24, 2023
Published: September 7, 2023

https://doi.org/10.1021/acs.macromol.3c00503
Macromolecules 2023, 56, 7320−7331

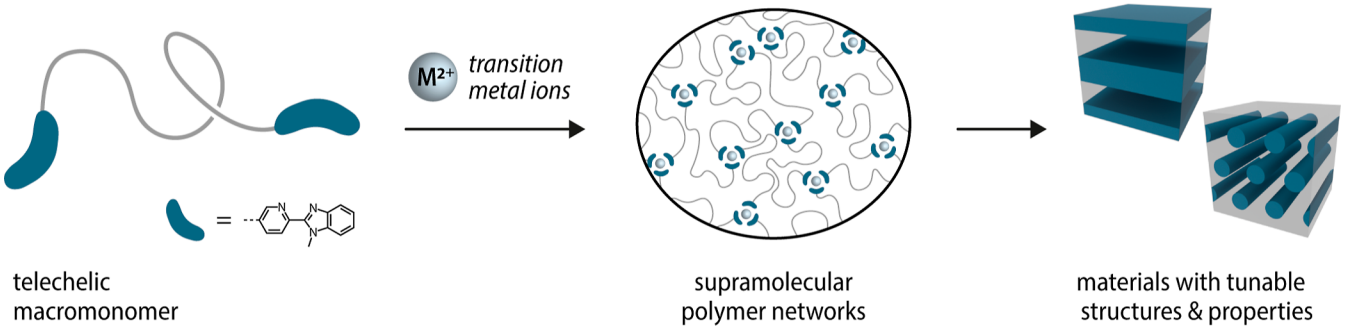

Figure 1. Schematic depiction of a telechelic macromonomer with methylbenzimidazolyl-pyridine ligands and its assembly with transition metal ions. The formation of threefold coordination complexes furnishes MSP networks, and the choice of metal ion influences the materials' structure and thermomechanical properties.

Scheme 1. Synthesis of (a) the Bidentate Ligand 1, the Low-Molecular-Weight Model Compound 2, and (b) the Telechelic, Ligand-Carrying PEB Macromonomer 3 ($M_n \approx 4000$ g mol^{-1}, $m \approx 0.39$, $n \approx 0.61$, $p \approx 62$)[a]

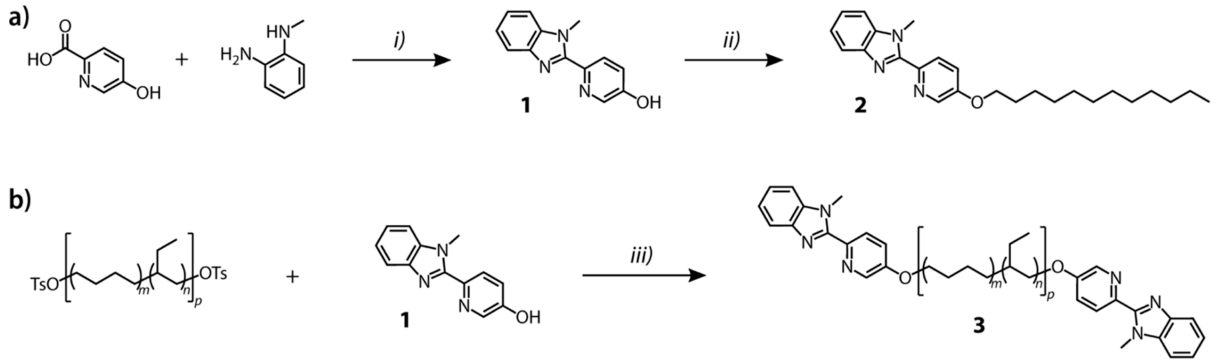

[a]Reagents and conditions: (i) H_3PO_4; (ii) 1-bromododecane, KOH, DMSO; and (iii) K_2CO_3, DMF/toluene 1:1 v/v.

branched, or dendritic structures upon complexation of strongly coordinating transition metal ions such as Ru(II) or Ir(II).[36−40] Additionally, metallosupramolecular assemblies of polymers that carry bipyridine, histidine, or related ligands in the backbone or as pendant groups have been explored, but the studies have mainly focused on investigating photophysical, photochemical, or catalytic properties.[40] Reports on the mechanical properties of MSPs with bidentate ligands include materials based on *N*-polyindoles,[41] polyurethanes,[12] or polydimethylsiloxanes,[22] all of which featured bipyridine units in the backbone and were noncovalently cross-linked by complex formation with transition metal ions or lanthanoids.[42] These studies have shown that the approach of embedding the ligand into the backbones of polymers allows one to create materials that span a broad range of properties. Intriguingly, however, few examples reported MSPs based on telechelic (macro)monomers featuring bidentate ligands, and these studies mostly focused on gels.[23,43−46]

With the aim to further expand the range of attainable properties of chain-extended MSP materials, we here report a new 6-(1′-methylbenzimidazolyl)-pyridin-3-ol (MBP) bidentate ligand (Figure 1), whose design and synthesis were inspired by the tridentate Mebip ligand.[47] The binding behavior of MBP with different transition metal ions was studied in solution by using a low-molecular-weight model compound. A telechelic macromonomer based on a poly(ethylene-*co*-butylene) (PEB) core and the MBP ligand at the two termini was synthesized and assembled into MSPs by the addition of different transition metal salts (Figure 1). The obtained polymeric materials were then subjected to a detailed investigation of the structure−property relationship in the solid state, showcasing how the latter are influenced by the choice of the metal ion.

RESULTS AND DISCUSSION

6-(1′-Methylbenzimidazolyl)-pyridin-3-ol **1** was prepared in good yield (44%) by the phosphoric acid-catalyzed condensation reaction of commercially available 5-hydroxypyridine-2-carboxylic acid and *N*-methyl-1,2-phenylenediamine (Scheme 1). A Williamson ether synthesis between **1** and 1-bromododecane was then carried out to access the low-molecular weight model compound **2**, while the PEB-based macromonomer **3** was synthesized by tosylation of bis(hydroxyl)-terminated PEB followed by nucleophilic substitution with **1**. Macromonomer **3** was obtained as a colorless, highly viscous liquid with a number-average molecular weight (M_n) of around 4000 g mol^{-1}, as determined by end-group analysis based on ^{1}H NMR spectroscopy. Size-exclusion chromatography (SEC) reveals an M_n of around 5500 g mol^{-1} for the original PEB and macromonomer **3** (Figure S1). The considerable discrepancy between the values determined via SEC and end-group analysis might originate from the assumption of complete functionalization, the inaccuracy of the SEC at such low molecular weights, and the difference from the employed polystyrene standard.

To explore the formation of metal−ligand complexes, UV−vis spectrophotometric titrations were carried out with model compound **2** instead of the polydisperse macromonomer **3** to achieve a high stoichiometric accuracy. Fe(OTf)$_2$, Zn(OTf)$_2$, and Ni(OTf)$_2$, which all feature the weakly coordinating

https://doi.org/10.1021/acs.macromol.3c00503
Macromolecules 2023, 56, 7320−7331

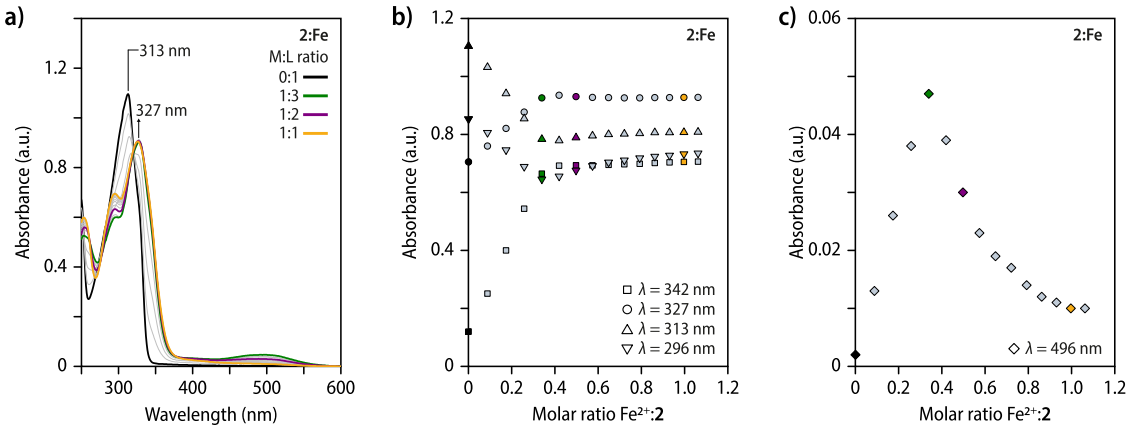

Figure 2. Spectrophotometric titrations of model compound **2** with solutions of iron(II) trifluoromethanesulfonate [$Fe(OTf)_2$]. (a) UV−vis absorption spectra of **2** (black line) acquired upon titration with aliquots of an $Fe(OTf)_2$ solution. (b) Plot of the absorbance at the absorption maximum of the free ligand (λ = 313 nm) and at wavelengths characteristic of the metal−ligand complexes (342, 327, and 296 nm) as a function of the metal-to-ligand (M/L) ratio. (c) Plot of the absorbance at λ = 496 nm against the M/L ratio, which shows a characteristic maximum at a 1:3 stoichiometry. Titrations were carried out with CH_3CN-solutions of **2** (c = 39.0 μmol L^{-1}) and $Fe(OTf)_2$ (c = 277 μmol L^{-1}).

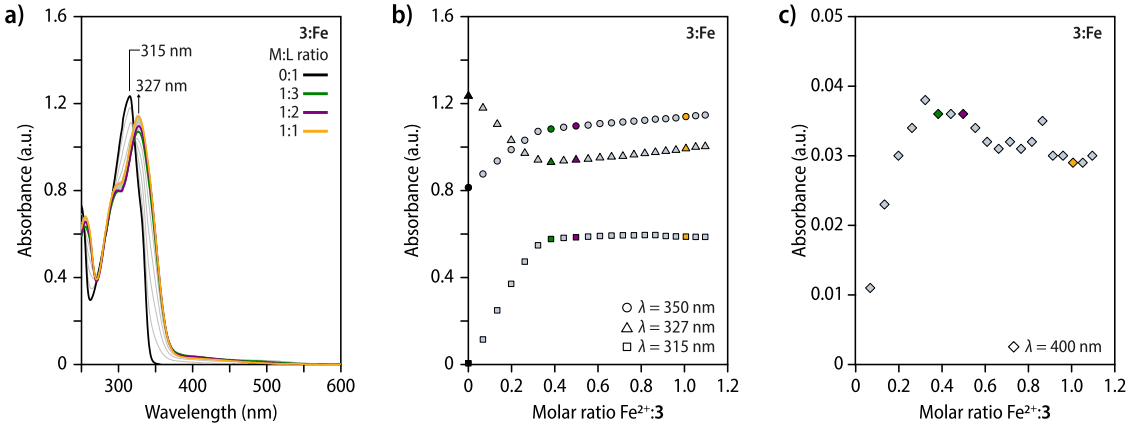

Figure 3. Spectrophotometric titrations of telechelic macromonomer **3** with $Fe(OTf)_2$. (a) UV−vis absorption spectra of **3** (black line) upon titration with aliquots of $Fe(OTf)_2$. (b) Plots of the absorbance at the absorption maximum of the free ligand (λ = 313 nm) and at the wavelength characteristic of the metal−ligand complex as a function of the metal-to-ligand (M/L) ratio. (c) Plot of the absorbance at λ = 400 nm, representative of the shoulder at higher wavelengths, against the M/L ratio. Titrations were carried out in $CHCl_3/CH_3CN$ (9:1 v/v) solutions of **3** (c = 23.9 μmol L^{-1}) and $Fe(OTf)_2$ (c = 299 μmol L^{-1}).

triflate counterion, were selected as the metal salts for these titrations (Figures 2 and S2). The UV−vis absorption spectra recorded upon addition of aliquots of a solution of $Fe(OTf)_2$ in CH_3CN (c = 277 μmol L^{-1}) to a solution of **2** [$c(CH_3CN)$ = 39.0 μmol L^{-1}] show a gradual decrease of the ligand's absorption band at 313 nm, which levels off at a metal-to-ligand (M/L) ratio of 1:3 (Figure 2a,b). A concomitant increase in a new band with a maximum at 327 nm was observed, which can be attributed to the formation of the corresponding metal−ligand charge−transfer complex. Plots of the absorbance against the M/L ratio show that the intensity of the band at 327 nm increases upon further addition of metal salt before leveling off at a M/L ratio of 1:3 (Figure 2b). Similar trends can be observed for absorbance changes at other wavelengths that are diagnostic for the ligand itself (313 nm) and for the formation of metal−ligand complexes (342 and 296 nm). In addition, an absorption band of weak intensity at 496 nm appears (Figure 2c), which shows a maximum at a 1:3 stoichiometry and decreases in intensity if the metal ion content is further increased, which might indicate that 1:2 complexes form if the amount of metal ions allows for it.[48]

Spectrophotometric titrations with **2** and metal salt solutions of $Zn(OTf)_2$ and $Ni(OTf)_2$ similarly show distinct bands indicative of a metal−ligand charge−transfer complex at 329 and 327 nm, respectively (Figure S2), albeit without a distinct absorption band at 496 nm. In both cases, the intensity of the bands associated with the metal−ligand complexes increases up to a 1:3 stoichiometry, and also at higher metal salt concentrations, the observations mirror those of the titrations with $Fe(OTf)_2$.

To further explore the binding behavior of the bidentate ligand, the data gained from spectrophotometric titrations were used to determine the binding constant of **2** with the respective metal ions (see the Supporting Information for details). Based on the data acquired under the specific conditions set forth above, the calculations reveal log(β) values of 15 for the **2:Zn**, while a log(β) of 18 was determined for the **2:Ni** and **2:Fe** complexes, with β as the overall binding constant between the metal ion and three ligands (Table S1).[49] In addition, the fitting protocol for the spectrophotometric data allows for the calculation of the respective absorption spectra of the metal−ligand complex species with different M/L ratios that form

https://doi.org/10.1021/acs.macromol.3c00503
Macromolecules 2023, 56, 7320−7331

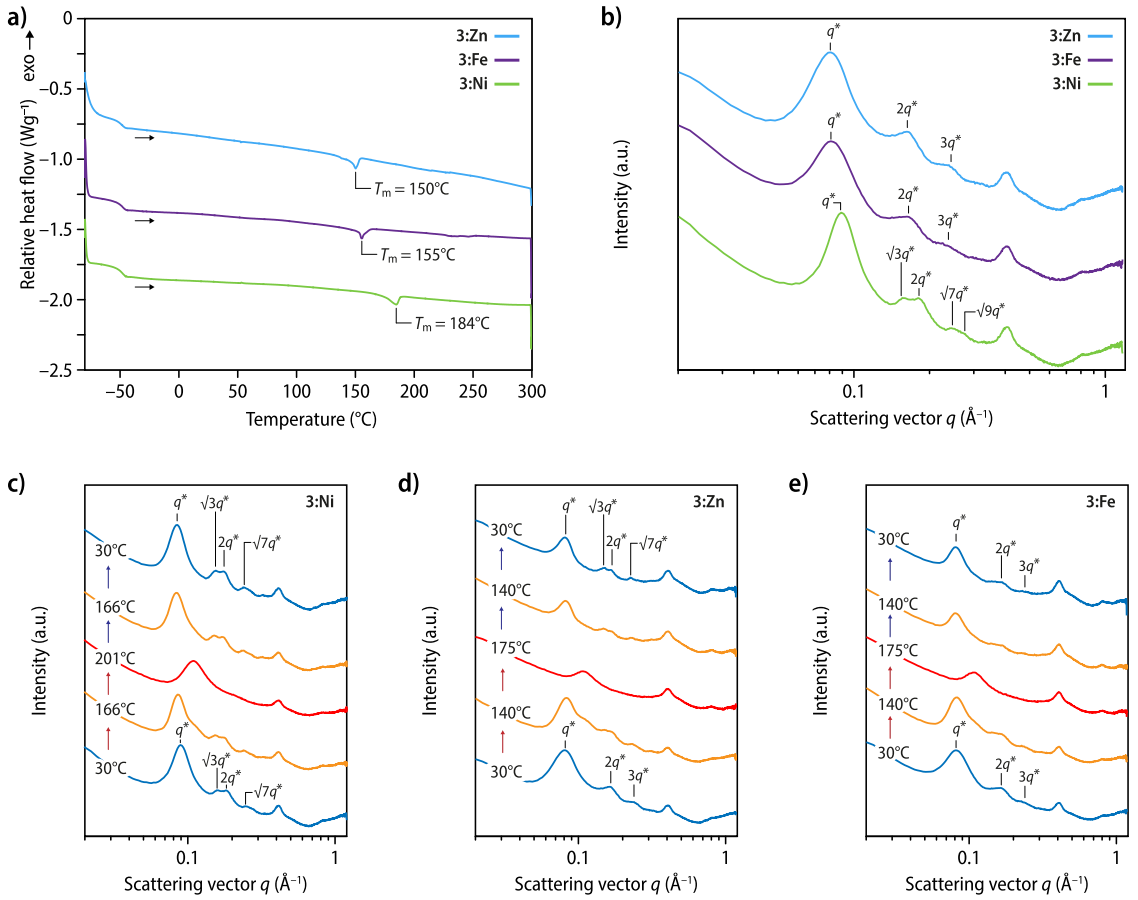

Figure 4. Thermal and structural characterizations of **3:Zn**, **3:Fe**, and **3:Ni**. Shown are representative (a) differential scanning calorimetry (DSC) traces (first heating), (b) small-angle X-ray scattering (SAXS) profiles, and (c–e) temperature-dependent SAXS profiles recorded between room temperature and upon heating above the melting transitions of the respective MSPs. DSC traces and SAXS profiles are shifted vertically for clarity and the main and higher order reflections are indicated. All spectra show a broad maximum at ca. 0.4 $Å^{-1}$ originating from the polyimide (Kapton) substrate used as a solid support.

throughout the titration (Figure S3) as well as their respective concentrations as a function of the M/L ratio (Figures S4 and S5). These calculations confirm that model compound **2** forms complexes with a 1:3 stoichiometry with the three investigated metal salts if the metal ion and ligand concentrations are adjusted to that ratio in solution. However, there seems to be a fraction of unbound ligand present at the stoichiometric concentration, especially in the case of **2:Zn** (Figure S5). At the same time, the analysis suggests that in addition to 1:3 complexes, complexes with 1:2 and 1:1 stoichiometries are present in solutions whose concentration has been adjusted for a M/L ratio of 1:3. Increasing the relative concentration of the metal salt then leads to a decrease of the fraction of 1:3 complexes and a shift of the equilibrium toward an increased fraction of bi- or monocomplexes.

To demonstrate that macromonomer **3** forms metal–ligand complexes in the same manner as model compound **2** and to adjust for a 1:3 M/L stoichiometry for the preparation of MSPs, additional spectrophotometric titrations of **3** with $Fe(OTf)_2$ were carried out (Figure 3). A solvent mixture of $CHCl_3/CH_3CN$ (9:1 v/v) was chosen in this case to ensure an adequate solubility of the apolar polymer, and aliquots of $Fe(OTf)_2$ (c = 299 μmol L^{-1}) were added to a solution of **3** (c = 23.9 μmol L^{-1}). The progression of the absorption spectra mirrors the behavior observed for the formation of **2:Fe** (Figure 3a). Similarly, plots of the absorption intensity at 315 nm, the absorption maximum of the free ligand, and at 327 nm, the previously determined absorption maximum of the metal–ligand complex, against the M/L ratio indicate that the complex formation with **3** occurs analogously (Figure 3b). Interestingly, the absorption spectrum is void of the low-energy band that is observed for the Fe^{2+}-complex of model compound **2** at 496 nm; instead, an extended shoulder with a maximum around 400 nm is observed, which gains in intensity until an M/L ratio of 1:3 is reached and becomes slightly less intense for higher M/L ratios (Figure 3c). The same experiment was repeated with $Zn(OTf)_2$ and similar results were obtained (Figure S6).

Films of the MSPs were then prepared by combining solutions of $Fe(OTf)_2$, $Zn(OTf)_2$, or $Ni(OTf)_2$ in MeOH (ca. 25 mmol L^{-1}) with solutions of **3** in $CHCl_3$ (ca. 5 mmol L^{-1}). Based on the spectrophotometric titrations of **3** discussed above, the quantities of the macromonomer and the metal salts were adjusted to a 1:3 M/L stoichiometry. For this purpose, the absorbance at λ = 327 nm was plotted as a function of the M/L ratio (Figure 3b), linear fits were applied to the two different regimes, and the intersection points of these fits were used to determine the amount of metal salt required to prepare MSPs. The analysis further allowed, under the assumption of complete end-functionalization of the PEB end-groups with MBP ligands, determination of the M_n of **3**. The value of ca. 3900 g mol^{-1} thus established matches the M_n determined by

https://doi.org/10.1021/acs.macromol.3c00503
Macromolecules 2023, 56, 7320–7331

^{1}H NMR spectroscopic end-group analysis. MSP solutions with an adjusted stoichiometry were then cast into poly(tetrafluoroethylene) Petri dishes. Upon evaporation of the solvents and further drying under vacuum at 50 °C, self-supporting films of **3:Zn** (colorless), **3:Fe** (red), and **3:Ni** (light blue) were obtained. To produce samples for further characterization, the solvent-cast MSPs were compression-molded at different temperatures below the melting transitions of the materials to obtain self-supporting films with a uniform thickness of about 200 μm (Figure S7, see the Supporting Information for processing details). Unless otherwise noted, all data were collected on compression-molded samples.

The thermal stability of all materials was analyzed via thermogravimetric analysis in air, and the recorded traces show a mass loss of 5 wt % for macromonomer **3** as well as all MSPs at around 392 °C (Figure S8). The thermal properties of **3** and the different MSPs were further investigated by differential scanning calorimetry (DSC). The first heating trace of **3** reveals a glass transition temperature (T_g) at around −45 °C. No additional transitions are observed, reflecting that **3** is amorphous (Figure S9 and Table S2). The first heating traces of all MSPs show a step-change in heat capacity at around −48 °C, corresponding to the T_g of the domains formed by the PEB segments and another endothermal transition at much higher temperatures, which is attributed to the melting of domains formed by the metal−ligand complexes (Figure 4a and Table S2). As previously reported,[6,20] the melting transitions (T_m) observed depend on the metal salt employed and range from 150 °C for **3:Zn** to 155 °C for **3:Fe** and 184 °C for **3:Ni**. The melting enthalpy is similar for all three MSPs with values between −2.4 and −3.4 J g^{-1}. Although the heats of fusion are unknown, the low melting enthalpies suggest that the extent of crystallinity in the MSP samples is relatively small. Second heating traces reflect that the melting and crystallization processes are completely reversible (Figure S10 and Table S2). To investigate the influence of the M/L stoichiometry and processing history on the thermal properties of the MPSs, **3:Zn** was chosen for in-depth studies. MSP samples with M/L ratios of 1:3, 1:2, and 1:1 were prepared by adjusting the corresponding stoichiometries in solution followed by solvent-casting and drying. The MSP films thus made were subjected to DSC measurements, which reveal that samples with a 1:2 M/L stoichiometry display a melting transition of ca. 120 °C, while a broad transition centered at ca. 80 is observed for samples with a 1:1 M/L stoichiometry (Figure S11). These findings strongly corroborate that MSPs for which a 1:3 M/L stoichiometry was adjusted in solution predominantly feature the corresponding coordination complexes in the solid state. To elucidate the role of the processing history, samples of **3:Zn** with a 1:3 M/L ratio were solution-casted, compression-molded at 140 °C and slowly cooled or quenched, or compression-molded at 160 °C, i.e., above the melting transition, followed by reprocessing at 140 °C and slow cooling (see the Supporting Information for details). A comparison of the recorded DSC traces shows that the highest melting enthalpy (−5.4 J g^{-1}) is observed for solution-cast samples (Figure S12 and Table S3). A more defined and pronounced melting transition is observed for samples that were heated above the melting transition and slowly cooled, but the melting enthalpy is, in fact, slightly lower (−4.0 J g^{-1}). Smaller differences are observed between slowly cooled and quenched samples when compression-molding was carried out at 140 °C. These findings suggest that the extent of crystallinity depends on the thermal history and is most pronounced, however still small, after solution-casting or processing from the melt.

To investigate the microstructure of the different MSPs, small- and wide-angle X-ray scattering (SAXS/WAXS) experiments were performed. In line with previous observations for related MSPs,[20,50−52] the scattering data show that microphase-separated morphologies form (Figure 4b and Table S4), presumably due to the polarity differences between the polymer backbone and the metal−ligand complexes. The SAXS diffractogram of **3:Ni** shows a Bragg peak at $q^* \approx 0.089$ Å^{-1} and higher order reflections at $\sqrt{3}q^*$, $2q^*$, $\sqrt{7}q^*$, and $3q^*$ (Figure 4b). This corroborates that **3:Ni** forms a hexagonal structure with a characteristic spacing of 7.06 nm, and a Scherrer analysis of the full-width-at-half-maximum (fwhm) of the main Bragg peak indicates a grain size of about 37.7 nm. Compared to **3:Ni**, the scattering profile of the **3:Fe** samples displays a broader main Bragg peak ($q^* \approx 0.081$ Å^{-1}) and integer higher-order reflections at $2q^*$ and $3q^*$ (Figure 4b), suggesting that a lamellar morphology forms. The analysis of the main Bragg peak indicates a characteristic spacing of 7.76 nm with a grain size of ca. 29.8 nm. The diffractogram of the **3:Zn** samples mirrors those of **3:Fe**, with a main Bragg reflection ($q^* \approx 0.080$ Å^{-1}) and higher higher-order reflections up to $3q^*$, indicative of a lamellar morphology (d = 7.85 nm) with a grain size of ca. 31.4 nm (Figure 4b). Thus, the SAXS data show that samples prepared with $Zn(OTf)_2$ and $Fe(OTf)_2$, at least when prepared using the casting/compression-molding protocol outlined above, develop a similar morphology, while the MSP assembled with $Ni(OTf)_2$ behaves differently. Even though melting and crystallization processes are observed by DSC, no distinct scattering peaks are observed in the WAXS regime for any of the samples, corroborating that the degree of crystallinity is very low, which is in accordance with the small melting and crystallization enthalpies observed for all materials (Figure S13).

In order to unequivocally correlate the thermal transitions observed by DSC with changes in the microstructure and to obtain further insights into microstructure formation, temperature-dependent SAXS measurements were performed with all three MSPs. Thus, samples were heated in 10 °C steps from 26 °C to above their respective melting temperature and were subsequently cooled to room temperature, also in 10 °C steps. SAXS measurements were carried out at each temperature after allowing for equilibration (see the Supporting Information for details). The scattering profiles of **3:Ni** samples recorded upon heating show a broadening of the main diffraction peak and the growth of an amorphous halo at ca. 0.109 Å^{-1} at around 166 °C, while a fully amorphous structure is observed above ca. 193 °C (Figures 4c and S14). Upon cooling, the first-order diffraction peak reappears at ca. 175 °C, and the diffraction pattern reveals that the hexagonal morphology is restored. In the case of **3:Zn**, the diffractograms recorded upon heating show that the development of an amorphous halo (0.107 Å^{-1}) starts at around 140 °C, and the loss of structural order occurs at a temperature of ca. 175 °C (Figures 4d and S15). Interestingly, the evolution of an additional scattering peak at $\sqrt{3}q^*$ is observed between 140 and 160 °C, suggesting a morphological rearrangement. Indeed, during cooling, the first order diffraction peak reappears at 166 °C and higher order reflections are observed at $\sqrt{3}q^*$, $2q^*$, and $\sqrt{7}q^*$, confirming that a hexagonal instead of a lamellar structure forms upon cooling from the melt. The morphological changes observed

https://doi.org/10.1021/acs.macromol.3c00503
Macromolecules 2023, 56, 7320−7331

for **3:Fe** qualitatively mirror those detected for **3:Zn**. The evolution of an amorphous halo (0.109 $Å^{-1}$) sets in around 140 °C, a new scattering peak at $\sqrt{3}q^*$ is observed between 140 and 150 °C, and amorphous samples are obtained at about 175 °C (Figures 4e and S16). Upon cooling from the melt, the main Bragg reflection reappears at ca. 166 °C and higher order diffraction peaks are observed at $\sqrt{3}q^*$, $2q^*$, and $\sqrt{7}q^*$, similarly hinting at the development of a hexagonal structure, although not as pronounced as for the **3:Zn** samples. For all materials, the temperature at which the microstructure starts to rearrange is ca. 10−20 °C below the melting transitions determined by DSC measurements, while full amorphization occurs at ca. 10−25 °C above the melting transitions. The position of the first-order diffraction peak is very different for **3:Ni** samples that were compression-molded or slowly cooled (over the course of several hours) from the melt; the diffractogram of the solution-cast sample shows an increased characteristic spacing (Figure S17a). By contrast, the position of the first-order diffraction peaks of **3:Zn** and **3:Fe** hardly depends on the processing history. For all three materials, the fwhm of the first-order diffraction is higher when samples were slowly cooled from the melt, indicating an increased grain size (Figure S17b).

The comparison of scattering profiles of samples that were recorded after quenching or slow cooling from the melt shows that in the case of **3:Zn** and **3:Fe**, the microstructure formation depends on the cooling rate. Samples that were slowly cooled adopt a hexagonal structure (Figure S18a and Table S5), while the diffractograms suggest a lamellar structure for quenched samples (Figure S18b and Table S5). By contrast, the diffractograms of samples of **3:Ni** show peaks indicative of a hexagonal structure, independent of the processing history (Figure S18a,b and Table S5). The first order diffraction peaks indicate a slightly decreased domain spacing for slowly cooled **3:Zn** and **3:Ni** samples, while no change is observed for **3:Fe** (Figure S18c and Table S5). Moreover, the analysis of the fwhm values of the main Bragg peaks shows that all slowly cooled samples display an improved long-range order compared to both quenched and pristine samples (Figure S18d and Table S5). Temperature-dependent WAXS measurements were also conducted, and the same scattering profiles are observed before and after the first heating and cooling cycle, suggesting that the low degree of crystallinity does not change appreciably with processing (Figure S19). In summary, these measurements show the correlation between the thermal transitions observed by DSC and the loss of microstructure, which leads to fully amorphous materials above the melting transition. Annealing effects could be observed for all materials. In the case of **3:Zn** and **3:Fe**, heating and slow cooling leads to increased grain sizes and a transformation from a lamellar into a hexagonal structure. These findings suggest that the lamellar microstructures are metastable and originate from kinetic trapping, while thermodynamically more favorable hexagonal structures are obtained upon slow cooling. For **3:Ni**, the reliable formation of a hexagonal structure was observed throughout. However, an increase in domain spacing is observed after the first heating cycle, as well as a larger grain size for slowly cooled samples. Differences in coordination geometry or crystallization characteristics of the different metal−ligand complexes possibly contribute to the observed differences in structure formation, but the absence of distinct WAXS peaks impedes further analysis.

To investigate how the choice of the metal salt influences the thermomechanical properties of the MSPs, dynamic mechanic analysis (DMA) in tension mode was performed on compression-molded films. All MSPs display comparable storage moduli (E') of around 1.4 to 1.7 GPa below −50 °C, i.e., in the glassy regime (Figure 5 and Table 1). The traces

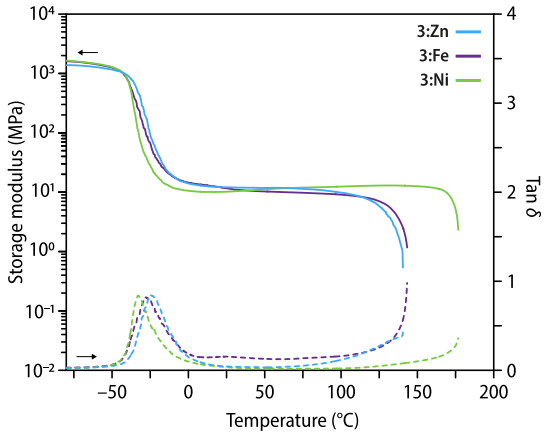

Figure 5. Thermomechanical characterization of **3:Zn**, **3:Fe**, and **3:Ni**. Shown is a comparison of representative dynamic mechanical analysis (DMA) traces (solid: storage modulus; dashed lines: tan δ).

show a drop in E' at around −30 °C, where all tan δ curves show a local maximum that is indicative of a glass transition associated with the phase formed by the PEB segments. The T_g determined from the local maxima in the tan δ traces is practically the same for the three MSPs and ranges from −26 ± 2 °C for **3:Zn** to −28 ± 0 °C for **3:Fe** and −32 ± 1 °C for **3:Ni** (Table 1). Above the T_g, flat rubbery plateaus are observed that extend up to the respective failure temperature (Figure 5), with little variation in E', which at room temperature assumes values between 11 and 13 MPa. The failure temperatures were found to be at 142 ± 1 and 143 ± 1 °C for **3:Zn** and **3:Fe**, respectively, and significantly higher for **3:Ni** with 177 ± 1 °C, which neatly correlates with the melting transitions observed by DSC (Figure 4a and Table S2). To probe if the thermal history influences the thermomechanical properties, films of **3:Zn** prepared using different processing protocols as explained above were characterized (Figure S20 and Table S6). As expected, considering the similar melting transitions observed in the respective DSC traces (Figure S12), the failure temperature of the different **3:Zn** samples is the same and no effect on E' is observed. In conclusion, the failure temperatures observed in DMA measurements of the different MSPs reflect the melting temperatures of the crystalline domains established by DSC, which indicates that the loss of these physical cross-links enables the materials to flow. This in turn suggests that any metallosupramolecular cross-links have dissociated or are highly dynamic at these temperatures.

To investigate the viscoelastic behavior of the different materials in more detail, frequency-dependent oscillatory shear rheology measurements in the linear regime were performed with macromonomer **3** as well as the three MSPs (Figures S21 and S22), while measurements with the PEB backbone have been previously reported.[20] First, a master curve was constructed from the acquired storage modulus (G'), loss modulus (G''), and loss factor (tan δ) for macromonomer **3** by time−temperature superposition (TTS) with a reference

https://doi.org/10.1021/acs.macromol.3c00503
Macromolecules 2023, 56, 7320−7331

Table 1. Thermal and Mechanical Properties of the MSPs

sample	T_g[a] (°C)	E' at 25 °C[a] (MPa)	failure temp.[a] (°C)	Young's modulus[b] (MPa)	tensile strength[b] (MPa)	strain at break[b] (%)	toughness[b] (kJ m^{-3})
3:Zn	−26 ± 2	13 ± 1	142 ± 1	11 ± 1	0.9 ± 0.1	12 ± 1	62 ± 34
3:Fe	−28 ± 0	12 ± 0.3	143 ± 2	9 ± 1	1.1 ± 0.1	23 ± 3	164 ± 40
3:Ni	−32 ± 1	11 ± 0.3	177 ± 1	9 ± 1	1.7 ± 0.2	41 ± 4	455 ± 26

[a]Data represent averages of n = 3 individual DMA measurements ± standard deviation. [b]Data represent averages of n = 4−5 individual uniaxial tensile tests ± standard deviation, measured at 25 °C with a strain rate of 15% min^{-1}.

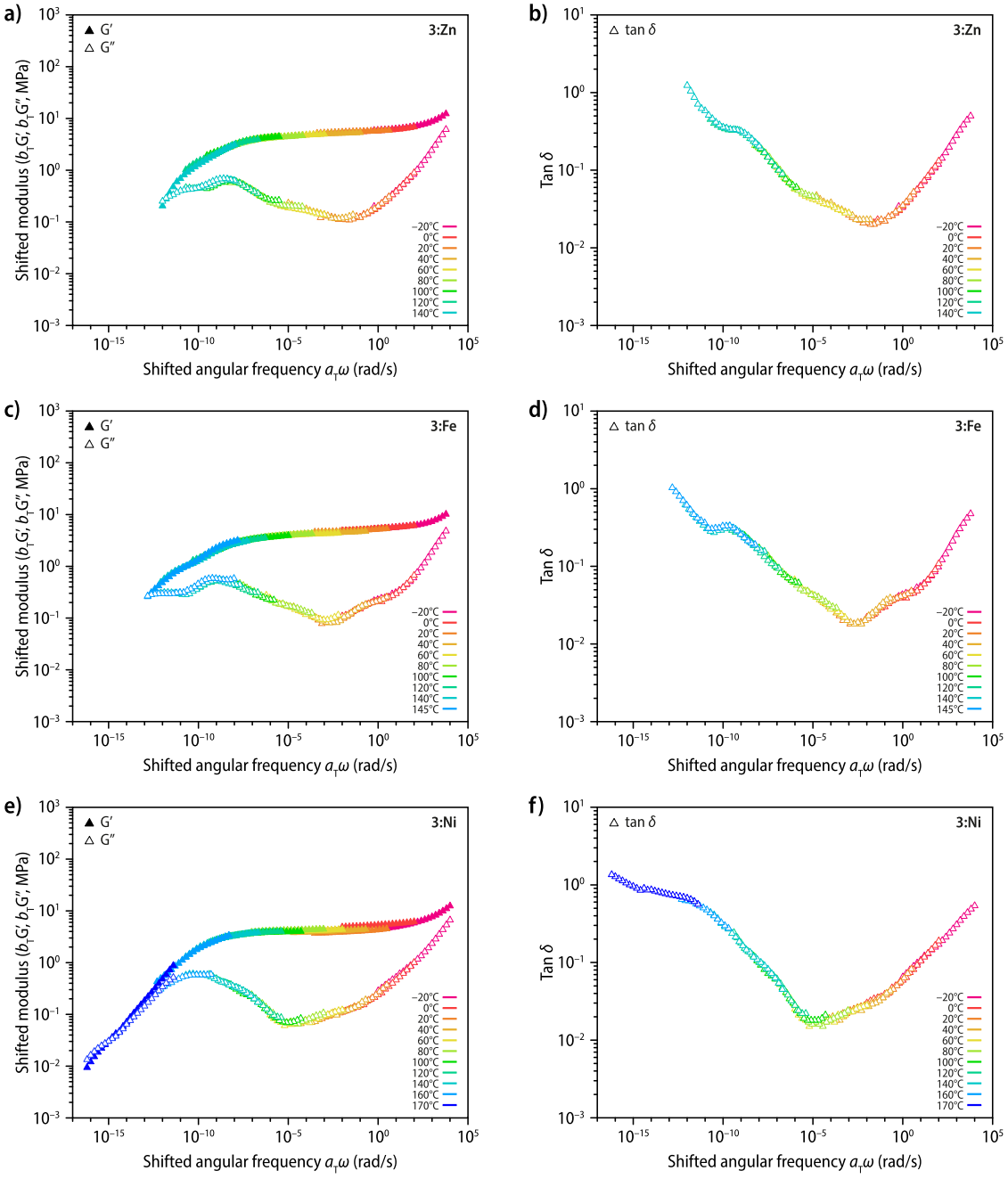

Figure 6. Linear shear rheologies of **3:Zn**, **3:Fe**, and **3:Ni**. Shown are master curves of (a,c,e) G' (filled triangle) and G'' (open triangle) and (b,d,f) tan δ at T_{ref} = 0 °C constructed by using manual horizontal (a_T) and vertical (b_T) shift factors shown in Figure S26.

temperature of 0 °C. The recorded curves for the loss factor at different temperatures were shifted horizontally (a_T) along the frequency axis until a good overlap was achieved (Figure S23b). The corresponding horizontal shift factors were fitted according to the Vogel−Fulcher−Tammann (VFT) eq (Figure S24b) and used to construct the G' and G'' master curves (Figure S23a).[53] Here, a good overlap was only achieved by applying additional vertical shift factors (b_T) to compensate for variations in the density of the sample and in chain mobility as a function of temperature, e.g., when passing through a phase

https://doi.org/10.1021/acs.macromol.3c00503
Macromolecules 2023, 56, 7320−7331

transition.[25] The constructed master curve shows a glassy regime with a storage modulus of around 150 MPa up to −40 °C, which is followed by a drop in G' that coincides with a local maximum in tan δ (Figure S23b). This is followed by terminal flow, which occurs at temperatures above ca. −20 °C. The observed transition at −40 °C can be attributed to the T_g of the PEB backbone, which was independently established by DSC and DMA measurements. These results suggest that macromonomer **3** behaves as an unentangled linear polymer melt. On the contrary, in the case of the three MSPs, the existing phase-separated structures are expected to increase the rheological complexity of the samples since different relaxation processes (i.e., macromonomer backbone, liquification of hard phases of crystallized ligands, and disassembly of ML complexes) are superimposed. To separate these effects, master curves of the MSPs (Figure S25) were first built by using the horizontal shift factors calculated for macromonomer **3** with high temperature values being extrapolated according to the VFT-fit (Figure S24). A good overlap of the curves can be observed below 20, 40, and 60 °C for **3:Zn**, **3:Fe**, and **3:Ni**, respectively, indicating that the relaxation processes in the materials below these temperatures are primarily dictated by the polymer backbone, while the supramolecular interactions are frozen. At higher temperatures, the master curves do not overlap anymore, suggesting the existence of other relaxation processes that start to significantly influence the viscoelastic behavior of the samples.

To elucidate the effect of the metal−ligand complexes, master curves for MSPs were then constructed by using manually determined horizontal as well as additional vertical shift factors (Figures 6 and S26). The master curve of **3:Zn** samples shows a rubbery plateau with a G' of around 5 MPa from −20 °C up to a temperature of 140 °C, where the crossover of G' and G'' occurs (Figure 6a). Within the rubbery plateau, the tan δ master curve shows an additional local maximum at around 40 °C (Figure 6b). For **3:Fe**, a rubbery plateau is observed between −20 and 140 °C, with G' around 4 MPa, before the crossover of G' and G'' is reached (Figure 6c). The tan δ master curve shows two local maxima at around 20 °C and weak maxima at 80 °C (Figure 6d). **3:Ni** displays the widest rubbery plateau with moduli around 4 MPa up to a temperature of ca. 160 °C, followed by a regime in which G' and G'' are parallel to each other until their crossover is reached at ca. 170 °C (Figure 6e). In contrast to **3:Zn** and **3:Fe**, no additional transitions are discernible in the tan δ curves (Figure 6f). For all MSPs, the crossover of G' and G'' correlates nicely with the melting transition observed by DSC, the failure temperature in DMA in tension, and the temperature regime in which structural changes are observed in the SAXS measurements. Taking these observations together, one can argue that the melting of the metal−ligand phase goes along with the transition from a more solid-like to a more liquid-like material due to the disintegration of the metal−ligand phase that reinforces the material below its T_m by providing physical cross-links. The gradual crossover of G' and G'' in the case of **3:Ni** could originate from the physical cross-linking provided by the microphase-separated structure with substantial long-range order, as previously observed for other supramolecular materials with aggregate-forming binding motifs.[54,55] The local maxima observed in the tan δ curves for **3:Zn** and **3:Fe** seem to reflect additional relaxation processes in these MSPs, which could be related to metal−ligand complexes in the amorphous polymer phase that become dynamic at lower temperatures.

Based on the data gained from rheological measurements, one can calculate the activation energy (E_a) for relaxation processes in different MSPs. For this purpose, the Arrhenius equation was fitted to the determined horizontal shift factors a_T vs 1000/T (Figure S27 and Table S7). The plots show the same slope up to a temperature of about 20 °C, which is in good agreement with the onset of the terminal flow regime for macromonomer **3**. This suggests that the mechanical properties of the MSPs are governed by the polymer backbone up to this temperature, and that the metal−ligand complexes are not (very) dynamic. Changes in the slope are observed for **3:Zn** and **3:Fe** at 40 and 60 °C, respectively, indicating that another relaxation mode is activated at these temperatures. Based on previous reports,[20] we speculate that this effect, which is not observed for **3:Ni**, is related to the relaxation of ML complexes that are not part of the microphase-separated domains and dynamically dissociate and reform. Another change in slope is observed at 120 °C for **3:Zn**, at 140 °C for **3:Fe**, and at 160 °C for **3:Ni**. These temperatures correspond to the temperatures where the crossover is reached, i.e., close to the observed melting transitions. The absence of a slope change for **3:Ni** below T_m parallels the absence of local maxima in the tan δ trace and can be explained by several factors. One possibility is that, in the case of **3:Ni**, fewer metal−ligand complexes reside in the amorphous polymer phase and that they are stabilized in an ML hard phase. This explanation is consistent with the increased long-range order of **3:Ni** observed by SAXS measurements. Another possibility is that MBP complexes with Ni^{2+} are less dynamic than those with Zn^{2+} and Fe^{2+}, so that their activation might coincide with the melting of a crystalline metal−ligand phase. Overall, one can conclude that the crossover, meaning the transition from a more solid to a more liquidlike material, correlates with the melting transition observed by DSC and failure in DMA measurements.

To further investigate the mechanical properties of the different MSPs, uniaxial tensile tests were performed at 25 °C with compression-molded samples at a strain rate of 15% min^{-1} (Figure 7 and Table 1). All materials show a brittle failure mode and comparable Young's moduli ranging from 9 ± 1 to 11 ± 1 MPa. The tensile strengths of **3:Zn** (0.9 ± 0.1 MPa) and **3:Fe** (1.1 ± 0.1 MPa) samples are comparable,

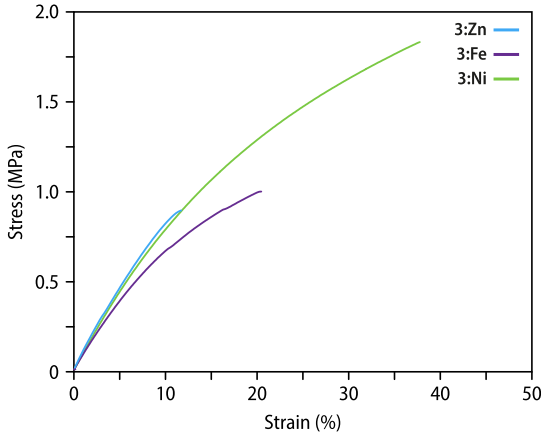

Figure 7. Mechanical characterization of samples of **3:Zn**, **3:Fe**, and **3:Ni**. Shown is a comparison of representative stress−strain curves acquired by uniaxial tensile testing.

https://doi.org/10.1021/acs.macromol.3c00503
Macromolecules 2023, 56, 7320−7331

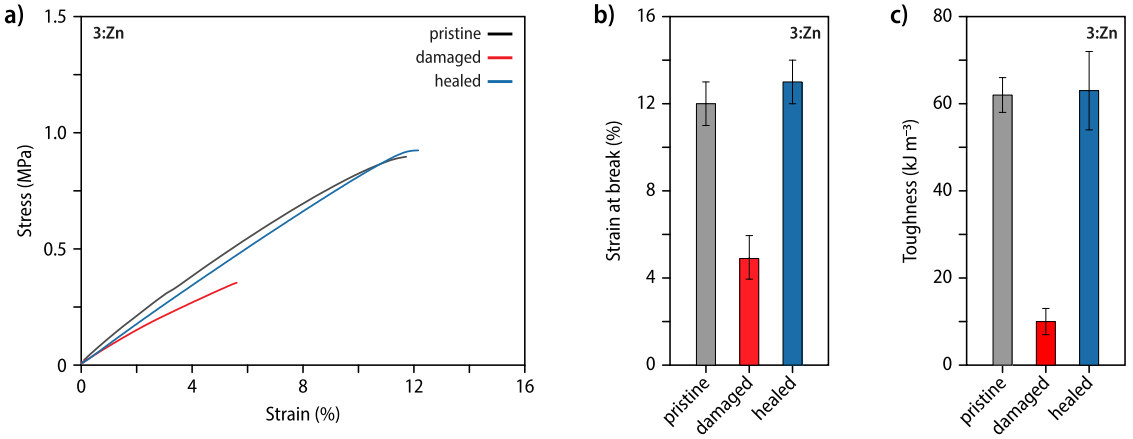

Figure 8. UV-light-induced healing of **3:Zn**. Shown are (a) the comparison of stress−strain curves measured by uniaxial tensile testing of pristine (gray), damaged (red), and healed (blue) samples, as well as a comparison of the values determined for (b) strain at break and (c) toughness of these samples. Error bars are the standard deviation calculated from 4−5 individual measurements.

whereas **3:Ni** samples display a significantly higher tensile strength of 1.7 ± 0.2 MPa. The strain at break increases from 12 ± 1% for the **3:Zn** samples to 23 ± 3% for **3:Fe** and 41 ± 4% for the **3:Ni** samples. Accordingly, the toughness is highest for **3:Ni** (455 ± 26 kJ m^{-3}), and lower for both **3:Fe** (164 ± 40 kJ m^{-3}) and **3:Zn** (62 ± 34 kJ m^{-3}) samples. The significantly higher extensibility and toughness of **3:Ni** in comparison to the other two MSPs are consistent with the increased long-range order, as determined by SAXS measurements, and a corresponding lower defect density in the microstructure, which can be assumed to increase the resistance to brittle failure. The influence of the processing history on the mechanical properties was exemplarily investigated for **3:Zn** (Figure S28 and Table S6). Thus, tensile tests were carried out with samples that were either heated above the melting transition of the metal−ligand phase to 160 °C and repressed at 140 °C or, alternatively, processed at 140 °C and either quenched or slowly cooled thereafter (see the Supporting Information of details). The differently processed samples show comparable properties, reflecting that the variation in processing conditions do not change the mechanical properties at ambient temperature appreciably, even if a slightly higher crystallinity was detected for slowly cooled samples.

On account of the dynamic nature of metal−ligand complexes, MSPs are known to be stimuli-responsive and can, in some cases, be healed.[6,50,56] To achieve this, samples can be heated to induce a temporary (local) depolymerization of the MSP or exposed to UV-light irradiation, which is absorbed and converted into heat. To demonstrate that MBP-based MSPs are a priori healable, the recovery of the mechanical properties of deliberately damaged samples of **3:Zn** was studied. Thus, samples with a thickness of around 200 μm were cut to 50% of their total depth with a razor blade, and the damaged area was exposed to UV-light of a wavelength between 320 and 390 nm for 30 s and an intensity of around 800 mW cm^{-2}. Monitoring of samples with an IR camera showed that the exposed area reached a temperature of around 150−160 °C, which causes the melting of the MSP and allows the material to flow. This enables the healing of the material with full recovery of the mechanical properties and the disappearance of the damage (Figures 8 and S29 and Table S8).

A closely related MSP with PEB as the backbone and the tridentate Mebip ligand at the termini was previously reported[6,20] and lends itself for a comparison to the properties of the MSPs reported herein. Assembling this macromonomer (BKB) with transition metal ions gives access to linearly chain-extended MSPs as complexes with a 1:2 M/L ratio form, while the addition of lanthanoid ions furnished 1:3 complexes that extend into a network structure, similar in architecture to the herein reported **3:Zn**, **3:Fe**, and **3:Ni** samples. Just like the latter, BKB samples with different lanthanoid salts displayed hexagonal as well as lamellar morphologies, while only lamellar structures were observed for linearly chain-extended MSP samples that featured stoichiometric complexes with transition metal ions.[20] While further investigations are required to unambiguously establish the relation between the employed building blocks and the morphology, the polymer architecture appears to exert a significant influence since only MSP networks with a 1:3 M/L ratio seem to form hexagonal structures. A significant difference between the MSPs with Mebip and MBP ligands is the much higher melting transitions of the crystalline domains of the former. For example, the herein reported MBP-MSPs display a melting transition of ca. 150 °C with $Zn(OTf_2)$ and 155 °C with $Fe(OTf_2)$, whereas BKB samples with the same metal salts were observed to feature melting transitions above 243 and 230 °C, respectively.[20] The difference may be associated with the smaller MBP ligands or the more complicated crystallization behavior of complexes with three coordinated ligands, as was similarly reported for Mebip complexes with lanthanoid ions of which only few crystallized.[20] Moreover, the high melting temperatures of Mebip-MSPs potentially impede efficient processing and limit their utility for practical applications, possibly rendering the MBP ligand an attractive alternative. A comparison of the mechanical properties of **3:Zn** and the related Mebip-based MSP shows a significantly higher toughness for the latter, with 62 ± 34 kJ m^{-3} versus 337 ± 100 kJ m^{-3}, as would be expected when comparing a cross-linked network with a linear polymer. Indeed, MSP networks formed by assembly of BKB with $La(NTf_2)_2$ display a toughness of 117 ± 5 kJ mol^{-1}, which is lower compared to the values observed for **3:Fe** (164 ± 40 kJ mol^{-1}) and **3:Ni** (455 ± 26 kJ mol^{-1}).[6] In terms of the ability of the MSPs to undergo stimulus-induced healing, it has been shown that

https://doi.org/10.1021/acs.macromol.3c00503
Macromolecules 2023, 56, 7320−7331

MSPs assembled from BKB and $La(NTf_2)_2$ or $Zn(NTf_2)_2$ only show a fast and full recovery upon UV-light irradiation if substoichiometric amounts of metal salt are used, which increases the dynamics but negatively affects the mechanical properties.[6] By contrast, the MSP bearing MPB as the ligand that was assembled with stoichiometric quantities of $Zn(OTf)_2$ shows excellent healing. These differences in the healing behavior of the MSPs appears closely related to the observed melting transitions of crystalline metal−ligand phases. In contrast to polymers that self-healing at ambient temperature, crystalline metal−ligand phases in MSPs effectively trap the complexes, restricting a dynamic rearrangement under ambient conditions.[56] Samples without a crystalline metal−ligand phase as for BKB and different lanthanoids[6,50] or with lower melting transitions as observed for **3:Zn** improve the healability significantly. Moreover, dangling ends caused by the use of substoichiometric amounts of the metal salt can also provide MSPs with a higher mobility to promote healing.[6,57] The comparison between these closely related MSPs highlights that an interplay of several factors including the ligand, metal salt, connectivity, and morphology determines the materials properties, allowing for the facile tuning of the properties, of such supramolecular polymers.

CONCLUSIONS

In summary, we here describe the synthesis of a bidentate ligand 6-(1′-methylbenzimidazolyl)-pyridin-3-ol (MBP), which as we show can serve as a building block for MSPs. The ligand forms complexes in a 1:3 ratio with $Zn(OTf)_2$, $Fe(OTf)_2$, and $Ni(OTf)_2$ so that the combination with MBP-functionalized telechelic macromonomers leads to assembly into supramolecular polymer networks. While a detailed analysis of the spectrophotometric titrations suggests that a minor fraction of complexes with a 1:2 and 1:1 ratio is present in dilute solutions of the three MSPs, the bulk samples appear to predominantly feature complexes with a 1:3 ratio. Nonetheless, the thermal transitions, microstructure, and (thermo)mechanical properties of these MSPs vary greatly with the employed metal ion. Thus, materials assembled with Zn^{2+} and Fe^{2+} behave similarly, while those assembled with Ni^{2+} show different properties. In all samples, melting transitions are observed that can be attributed to the presence of crystalline domains formed by the metal−ligand complexes, with a melting transition of 184 °C for **3:Ni** and lower transitions of 150 and 155 °C for **3:Zn** and **3:Fe**, respectively. SAXS reveals a hexagonal morphology for **3:Ni**, while the scattering profiles of **3:Zn** and **3:Fe** suggest a lamellar structure for samples compression-molded below the respective melting transition. Upon heating, the microstructure starts to change around 10−20 °C below the melting transition, with full amorphization upon further heating. Annealing at elevated temperatures leads to the formation of **3:Zn** and **3:Fe** with a hexagonal morphology, while quenching of samples from the melt appears to yield a lamellar morphology. DMA and shear rheology measurements indicate that the melting of crystalline domains and subsequent amorphization of the materials is associated with a loss of physical cross-links, allowing the materials to flow. Moreover, the master curves obtained by time−temperature superposition indicate that additional relaxation processes at lower temperatures occur for **3:Zn** and **3:Fe** samples, which can be attributed to dynamic relaxation of metal−ligand complexes that are not part of crystalline domains. This was, however, not observed for **3:Ni**, and the absence of dynamic relaxation processes in these samples may be due to the comparatively high order of the microstructure in this material. With regard to the mechanical properties at ambient temperature, all materials show a similar stiffness, while the strain at break and toughness vary greatly. Samples of **3:Ni** display the highest extensibility and toughness, which can be again related to the increased long-range order, which might be beneficial for the resistance of the material toward brittle failure. Lastly, the ability of the materials to heal was investigated using **3:Zn** as a model system. Exposure of damaged samples to UV-light followed by uniaxial tensile testing served to demonstrate that recovery of the mechanical properties is possible. A comparison of the materials properties with analogous MSPs carrying the established Mebip ligand shows, that the melting transition of the here investigated material is significantly decreased,[20] which might be the decisive factor for their improved healability,[6] making this new ligand an intriguing new building block for such materials with responsive properties.

ASSOCIATED CONTENT

Data Availability Statement

The source data of this study are available from the Zenodo repository at: https://doi.org/10.5281/zenodo.8308077.

Supporting Information

The Supporting Information is available free of charge at https://pubs.acs.org/doi/10.1021/acs.macromol.3c00503.

Detailed description of the materials, experimental methods, synthetic procedures, and analytical data for all compounds (PDF)

AUTHOR INFORMATION

Corresponding Authors

Christoph Weder − *Adolphe Merkle Institute, University of Fribourg, 1700 Fribourg, Switzerland;* orcid.org/0000-0001-7183-1790; Email: christoph.weder@unifr.ch

Stephen Schrettl − *Adolphe Merkle Institute, University of Fribourg, 1700 Fribourg, Switzerland; TUM School of Life Sciences, Technical University of Munich, 85354 Freising, Germany;* orcid.org/0000-0002-6371-3089; Email: stephen.schrettl@tum.de

Authors

Franziska Marx − *Adolphe Merkle Institute, University of Fribourg, 1700 Fribourg, Switzerland*

Malte Beccard − *Adolphe Merkle Institute, University of Fribourg, 1700 Fribourg, Switzerland*

Alessandro Ianiro − *Adolphe Merkle Institute, University of Fribourg, 1700 Fribourg, Switzerland;* orcid.org/0000-0003-4709-4350

Andrea Dodero − *Adolphe Merkle Institute, University of Fribourg, 1700 Fribourg, Switzerland*

Laura N. Neumann − *Adolphe Merkle Institute, University of Fribourg, 1700 Fribourg, Switzerland*

Grégory Stoclet − *Univ. Lille, CNRS, INRAE, Centrale Lille, UMR 8207—UMET—Unité Matériaux et Transformations, F-59000 Lille, France*

Complete contact information is available at: https://pubs.acs.org/10.1021/acs.macromol.3c00503

Notes

The authors declare no competing financial interest.

https://doi.org/10.1021/acs.macromol.3c00503
Macromolecules 2023, 56, 7320−7331

■ ACKNOWLEDGMENTS

We gratefully acknowledge financial support through the National Center of Competence in Research Bio-Inspired Materials, a research instrument of the Swiss National Science Foundation (SNF). The worked described herein was also supported by funding though the Swiss National Science Foundation (grant no. 200020_172619) and the Adolphe Merkle Foundation. Anton Paar GmbH is gratefully acknowledged for the loan of the MCR702 MultiDrive rheometer and their excellent technical support. We thank Dr. Michael Fischer for help with the schematic depiction of the morphology.

■ REFERENCES

(1) Sijbesma, R. P.; Beijer, F. H.; Brunsveld, L.; Folmer, B. J. B.; Hirschberg, J. H. K. K.; Lange, R. F. M.; Lowe, J. K. L.; Meijer, E. W. Reversible Polymers Formed from Self-Complementary Monomers Using Quadruple Hydrogen Bonding. *Science* **1997**, *278* (5343), 1601−1604.

(2) Yang, L.; Tan, X.; Wang, Z.; Zhang, X. Supramolecular Polymers: Historical Development, Preparation, Characterization, and Functions. *Chem. Rev.* **2015**, *115* (15), 7196−7239.

(3) Aida, T.; Meijer, E. W.; Stupp, S. I. Functional Supramolecular Polymers. *Science* **2012**, *335* (6070), 813−817.

(4) Herbert, K. M.; Schrettl, S.; Rowan, S. J.; Weder, C. 50th Anniversary Perspective: Solid-State Multistimuli, Multiresponsive Polymeric Materials. *Macromolecules* **2017**, *50* (22), 8845−8870.

(5) Yan, X.; Wang, F.; Zheng, B.; Huang, F. Stimuli-Responsive Supramolecular Polymeric Materials. *Chem. Soc. Rev.* **2012**, *41* (18), 6042−6065.

(6) Burnworth, M.; Tang, L.; Kumpfer, J. R.; Duncan, A. J.; Beyer, F. L.; Fiore, G. L.; Rowan, S. J.; Weder, C. Optically Healable Supramolecular Polymers. *Nature* **2011**, *472* (7343), 334−337.

(7) Campanella, A.; Döhler, D.; Binder, W. H. Self-Healing in Supramolecular Polymers. *Macromol. Rapid Commun.* **2018**, *39* (17), 1700739.

(8) Sautaux, J.; Montero de Espinosa, L.; Balog, S.; Weder, C. Multistimuli, Multiresponsive Fully Supramolecular Orthogonally Bound Polymer Networks. *Macromolecules* **2018**, *51* (15), 5867−5874.

(9) Neumann, L. N.; Weder, C.; Schrettl, S. Healing of Polymeric Solids by Supramolecular Means. *Chimia* **2019**, *73* (4), 277−282.

(10) Hohl, D. K.; Weder, C. (De)Bonding on Demand with Optically Switchable Adhesives. *Adv. Opt. Mater.* **2019**, *7* (16), 1900230.

(11) Heinzmann, C.; Weder, C.; de Espinosa, L. M. Supramolecular Polymer Adhesives: Advanced Materials Inspired by Nature. *Chem. Soc. Rev.* **2016**, *45* (2), 342−358.

(12) Wang, X.; Zhan, S.; Lu, Z.; Li, J.; Yang, X.; Qiao, Y.; Men, Y.; Sun, J. Healable, Recyclable, and Mechanically Tough Polyurethane Elastomers with Exceptional Damage Tolerance. *Adv. Mater.* **2020**, *32* (50), 2005759.

(13) Wang, C.; Yang, L.; Chang, G. Recyclable Cu(II)-Coordination Crosslinked Poly(Benzimidazolyl Pyridine)s as High-Performance Polymers. *Macromol. Rapid Commun.* **2018**, *39* (6), 1700573.

(14) Knapton, D.; Iyer, P. K.; Rowan, S. J.; Weder, C. Synthesis and Properties of Metallo-Supramolecular Poly(*p* -Xylylene)s. *Macromolecules* **2006**, *39* (12), 4069−4075.

(15) Knapton, D.; Rowan, S. J.; Weder, C. Synthesis and Properties of Metallo-Supramolecular Poly(*p* -Phenylene Ethynylene)s. *Macromolecules* **2006**, *39* (2), 651−657.

(16) Balkenende, D. W. R.; Olson, R. A.; Balog, S.; Weder, C.; Montero de Espinosa, L. Epoxy Resin-Inspired Reconfigurable Supramolecular Networks. *Macromolecules* **2016**, *49* (20), 7877−7885.

(17) Winter, A.; Schubert, U. S. Synthesis and Characterization of Metallo-Supramolecular Polymers. *Chem. Soc. Rev.* **2016**, *45* (19), 5311−5357.

(18) Whittell, G. R.; Hager, M. D.; Schubert, U. S.; Manners, I. Functional Soft Materials from Metallopolymers and Metallosupramolecular Polymers. *Nat. Mater.* **2011**, *10* (3), 176−188.

(19) Beck, J. B.; Ineman, J. M.; Rowan, S. J. Metal/Ligand-Induced Formation of Metallo-Supramolecular Polymers. *Macromolecules* **2005**, *38* (12), 5060−5068.

(20) Neumann, L. N.; Gunkel, I.; Barron, A.; Oveisi, E.; Petzold, A.; Thurn-Albrecht, T.; Schrettl, S.; Weder, C. Structure-Property Relationships of Microphase-Separated Metallosupramolecular Polymers. *Macromolecules* **2020**, *53* (13), 5068−5084.

(21) Burnworth, M.; Knapton, D.; Rowan, S. J.; Weder, C. Metallo-Supramolecular Polymerization: A Route to Easy-To-Process Organic/Inorganic Hybrid Materials. *J. Inorg. Organomet. Polym. Mater.* **2007**, *17* (1), 91−103.

(22) Rao, Y.-L.; Chortos, A.; Pfattner, R.; Lissel, F.; Chiu, Y.-C.; Feig, V.; Xu, J.; Kurosawa, T.; Gu, X.; Wang, C.; He, M.; Chung, J. W.; Bao, Z. Stretchable Self-Healing Polymeric Dielectrics Cross-Linked Through Metal-Ligand Coordination. *J. Am. Chem. Soc.* **2016**, *138* (18), 6020−6027.

(23) Ahmadi, M.; Seiffert, S. Coordination Geometry Preference Regulates the Structure and Dynamics of Metallo-Supramolecular Polymer Networks. *Macromolecules* **2021**, *54* (3), 1388−1400.

(24) Wojtecki, R. J.; Nelson, A. Small Changes with Big Effects: Tuning Polymer Properties with Supramolecular Interactions. *J. Polym. Sci., Part A: Polym. Chem.* **2016**, *54* (4), 457−472.

(25) Kumpfer, J. R.; Wie, J. J.; Swanson, J. P.; Beyer, F. L.; Mackay, M. E.; Rowan, S. J. Influence of Metal Ion and Polymer Core on the Melt Rheology of Metallosupramolecular Films. *Macromolecules* **2012**, *45* (1), 473−480.

(26) Schubert, U. S.; Newkome, G. R.; Winter, A. *Supramolecular Polymers and Assemblies*, 1st ed.; Wiley VCH, 2021.

(27) Dobrawa, R.; Würthner, F. Metallosupramolecular Approach toward Functional Coordination Polymers. *J. Polym. Sci., Part A: Polym. Chem.* **2005**, *43* (21), 4981−4995.

(28) Zhao, J.; Yuan, J.; Fang, Z.; Huang, S.; Chen, Z.; Qiu, F.; Lu, C.; Zhu, J.; Zhuang, X. One-Dimensional Coordination Polymers Based on Metal-Nitrogen Linkages. *Coord. Chem. Rev.* **2022**, *471*, 214735.

(29) Shunmugam, R.; Gabriel, G. J.; Aamer, K. A.; Tew, G. N. Metal-Ligand-Containing Polymers: Terpyridine as the Supramolecular Unit. *Macromol. Rapid Commun.* **2010**, *31* (9−10), 784−793.

(30) Housecroft, C. E.; Constable, E. C. Isomers of Terpyridine as Ligands in Coordination Polymers and Networks Containing Zinc(II) and Cadmium(II). *Molecules* **2021**, *26* (11), 3110.

(31) Chiper, M.; Hoogenboom, R.; Schubert, U. S. Toward Main Chain Metallo-Terpyridyl Supramolecular Polymers: "The Metal Does the Trick. *Macromol. Rapid Commun.* **2009**, *30* (8), 565−578.

(32) Dobrawa, R.; Würthner, F. Metallosupramolecular Approach toward Functional Coordination Polymers. *J. Polym. Sci., Part A: Polym. Chem.* **2005**, *43* (21), 4981−4995.

(33) Tang, S.; Olsen, B. D. Relaxation Processes in Supramolecular Metallogels Based on Histidine-Nickel Coordination Bonds. *Macromolecules* **2016**, *49* (23), 9163−9175.

(34) Yount, W. C.; Loveless, D. M.; Craig, S. L. Small-Molecule Dynamics and Mechanisms Underlying the Macroscopic Mechanical Properties of Coordinatively Cross-Linked Polymer Networks. *J. Am. Chem. Soc.* **2005**, *127* (41), 14488−14496.

(35) Yount, W. C.; Loveless, D. M.; Craig, S. L. Strong Means Slow: Dynamic Contributions to the Bulk Mechanical Properties of Supramolecular Networks. *Angew. Chem., Int. Ed.* **2005**, *44* (18), 2746−2748.

(36) Campagna, S.; Denti, G.; Serroni, S.; Juris, A.; Venturi, M.; Ricevuto, V.; Balzani, V. Dendrimers of Nanometer Size Based on Metal Complexes: Luminescent and Redox-Active Polynuclear Metal Complexes Containing up to Twenty-Two Metal Centers. *Chem.—Eur. J.* **1995**, *1* (4), 211−221.

(37) Serroni, S.; Denti, G.; Campagna, S.; Juris, A.; Ciano, M.; Balzani, V. Arborols Based on Luminescent and Redox-Active

https://doi.org/10.1021/acs.macromol.3c00503
Macromolecules 2023, 56, 7320−7331

Transition Metal Complexes. *Angew. Chem., Int. Ed. Engl.* **1992**, *31* (11), 1493−1495.
(38) Kelch, S.; Rehahn, M. High-Molecular-Weight Ruthenium(II) Coordination Polymers: Synthesis and Solution Properties. *Macromolecules* **1997**, *30* (20), 6185−6193.
(39) Knapp, R.; Schott, A.; Rehahn, M. A Novel Synthetic Strategy toward Soluble, Well-Defined Ruthenium(II) Coordination Polymers. *Macromolecules* **1996**, *29* (1), 478−480.
(40) Schubert, U. S.; Eschbaumer, C. Macromolecules Containing Bipyridine and Terpyridine Metal Complexes: Towards Metallosupramolecular Polymers. *Angew. Chem., Int. Ed.* **2002**, *41* (16), 2892−2926.
(41) Chang, G.; Wang, C.; Du, M.; Liu, S.; Yang, L. Metal-Coordination Crosslinked N-Polyindoles as Recyclable High-Performance Thermosets and Nondestructive Detection for Their Tensile Strength and Glass Transition Temperature. *Chem. Commun.* **2018**, *54* (23), 2906−2909.
(42) Rao, Y.-L.; Feig, V.; Gu, X.; Nathan Wang, G. J.; Bao, Z. The Effects of Counter Anions on the Dynamic Mechanical Response in Polymer Networks Crosslinked by Metal-Ligand Coordination. *J. Polym. Sci., Part A: Polym. Chem.* **2017**, *55* (18), 3110−3116.
(43) Grindy, S. C.; Lenz, M.; Holten-Andersen, N. Engineering Elasticity and Relaxation Time in Metal-Coordinate Cross-Linked Hydrogels. *Macromolecules* **2016**, *49* (21), 8306−8312.
(44) Fullenkamp, D. E.; He, L.; Barrett, D. G.; Burghardt, W. R.; Messersmith, P. B. Mussel-Inspired Histidine-Based Transient Network Metal Coordination Hydrogels. *Macromolecules* **2013**, *46* (3), 1167−1174.
(45) Tang, Q.; Zhao, D.; Zhou, Q.; Yang, H.; Peng, K.; Zhang, X. Polyhistidine-Based Metal Coordination Hydrogels with Physiologically Relevant PH Responsiveness and Enhanced Stability through a Novel Synthesis. *Macromol. Rapid Commun.* **2018**, *39* (11), 1800109.
(46) Rossow, T.; Bayer, S.; Albrecht, R.; Tzschucke, C. C.; Seiffert, S. Supramolecular Hydrogel Capsules Based on PEG: A Step Toward Degradable Biomaterials with Rational Design. *Macromol. Rapid Commun.* **2013**, *34* (17), 1401−1407.
(47) Rowan, S. J.; Beck, J. B. Metal-Ligand Induced Supramolecular Polymerization : A Route to Responsive Materials. *Faraday Discuss.* **2005**, *128* (0), 43−53.
(48) Holyer, R. H.; Hubbard, C. D.; Kettle, S. F. A.; Wilkins, R. G. The Kinetics of Replacement Reactions of Complexes of the Transition Metals with 1,10-Phenanthroline and 2,2'-Bipyridine. *Inorg. Chem.* **1965**, *4* (7), 929−935.
(49) Piguet, C.; Bernardinelli, G.; Bocquet, B.; Quattropani, A.; Williams, A. F. Self-Assembly of Double and Triple Helices Controlled by Metal Ion Stereochemical Preference. *J. Am. Chem. Soc.* **1992**, *114* (19), 7440−7451.
(50) Neumann, L. N.; Oveisi, E.; Petzold, A.; Style, R. W.; Thurn-Albrecht, T.; Weder, C.; Schrettl, S. Dynamics and Healing Behavior of Metallosupramolecular Polymers. *Sci. Adv.* **2021**, *7* (18), No. eabe4154.
(51) Sautaux, J. *Stimuli-Responsive Supramolecular Networks*; University of Fribourg: Fribourg, 2019.
(52) Ghiassinejad, S.; Mortensen, K.; Rostamitabar, M.; Malineni, J.; Fustin, C.-A.; van Ruymbeke, E. Dynamics and Structure of Metallo-Supramolecular Polymers Based on Short Telechelic Precursors. *Macromolecules* **2021**, *54* (13), 6400−6416.
(53) Fulcher, G. S. Analysis of Recent Measurements of the Viscosity of Glasses. *J. Am. Ceram. Soc.* **1925**, *8* (6), 339−355.
(54) Golkaram, M.; Loos, K. A Critical Approach to Polymer Dynamics in Supramolecular Polymers. *Macromolecules* **2019**, *52* (24), 9427−9444.
(55) Ahmadi, M.; Hawke, L. G. D.; Goldansaz, H.; van Ruymbeke, E. Dynamics of Entangled Linear Supramolecular Chains with Sticky Side Groups: Influence of Hindered Fluctuations. *Macromolecules* **2015**, *48* (19), 7300−7310.
(56) Li, B.; Cao, P.-F.; Saito, T.; Sokolov, A. P. Intrinsically Self-Healing Polymers: From Mechanistic Insight to Current Challenges. *Chem. Rev.* **2023**, *123* (2), 701−735.
(57) Li, Y.; Pyromali, C.; Zhuge, F.; Fustin, C.-A.; Gohy, J.-F.; Vlassopoulos, D.; van Ruymbeke, E. Dynamics of Entangled Metallosupramolecular Polymer Networks Combining Stickers with Different Lifetimes. *J. Rheol.* **2022**, *66* (6), 1203−1220.

https://doi.org/10.1021/acs.macromol.3c00503
Macromolecules 2023, 56, 7320−7331